

EUROPEAN LABORATORY FOR PARTICLE PHYSICS

CERN-PPE/97-087

18 July 1997

Measurement of the Q^2 evolution of the photon structure function F_2^γ

The OPAL Collaboration

Abstract

New measurements are presented of the photon structure function $F_2^\gamma(x, Q^2)$ at four values of Q^2 between 9 and 59 GeV^2 based on data collected with the OPAL detector at centre-of-mass energies of 161–172 GeV, with a total integrated luminosity of 18.1 pb^{-1} . The evolution of F_2^γ with Q^2 in bins of x is determined in the Q^2 range from 1.86 to 135 GeV^2 using data taken at centre-of-mass energies of 91 GeV and 161–172 GeV. F_2^γ is observed to increase with Q^2 with a slope of $\alpha^{-1} dF_2^\gamma / d \ln Q^2 = 0.10_{-0.03}^{+0.05}$ measured in the range $0.1 < x < 0.6$.

(Submitted to Physics Letters B)

arXiv:hep-ex/9708019v1 16 Aug 1997

The OPAL Collaboration

K. Ackerstaff⁸, G. Alexander²³, J. Allison¹⁶, N. Altekamp⁵, K.J. Anderson⁹,
S. Anderson¹², S. Arcelli², S. Asai²⁴, D. Axen²⁹, G. Azuelos^{18,a}, A.H. Ball¹⁷,
E. Barberio⁸, T. Barillari², R.J. Barlow¹⁶, R. Bartoldus³, J.R. Batley⁵, S. Baumann³,
J. Bechtluft¹⁴, C. Beeston¹⁶, T. Behnke⁸, A.N. Bell¹, K.W. Bell²⁰, G. Bella²³,
S. Bentvelsen⁸, S. Bethke¹⁴, O. Biebel¹⁴, A. Biguzzi⁵, S.D. Bird¹⁶, V. Blobel²⁷,
I.J. Bloodworth¹, J.E. Bloomer¹, M. Bobinski¹⁰, P. Bock¹¹, D. Bonacorsi²,
M. Boutemur³⁴, B.T. Bouwens¹², S. Braibant¹², L. Brigliadori², R.M. Brown²⁰,
H.J. Burckhart⁸, C. Burgard⁸, R. Bürgin¹⁰, P. Capiluppi², R.K. Carnegie⁶,
A.A. Carter¹³, J.R. Carter⁵, C.Y. Chang¹⁷, D.G. Charlton^{1,b}, D. Chrisman⁴,
P.E.L. Clarke¹⁵, I. Cohen²³, J.E. Conboy¹⁵, O.C. Cooke⁸, M. Cuffiani², S. Dado²²,
C. Dallapiccola¹⁷, G.M. Dallavalle², R. Davies³⁰, S. De Jong¹², L.A. del Pozo⁴,
K. Desch³, B. Dienes^{33,d}, M.S. Dixit⁷, E. do Couto e Silva¹², M. Doucet¹⁸,
E. Duchovni²⁶, G. Duckeck³⁴, I.P. Duerdoth¹⁶, D. Eatough¹⁶, J.E.G. Edwards¹⁶,
P.G. Estabrooks⁶, H.G. Evans⁹, M. Evans¹³, F. Fabbri², M. Fanti², A.A. Faust³⁰,
F. Fiedler²⁷, M. Fierro², H.M. Fischer³, I. Fleck⁸, R. Folman²⁶, D.G. Fong¹⁷,
M. Foucher¹⁷, A. Fürttjes⁸, D.I. Futyan¹⁶, P. Gagnon⁷, J.W. Gary⁴, J. Gascon¹⁸,
S.M. Gascon-Shotkin¹⁷, N.I. Geddes²⁰, C. Geich-Gimbel³, T. Geralis²⁰, G. Giacomelli²,
P. Giacomelli⁴, R. Giacomelli², V. Gibson⁵, W.R. Gibson¹³, D.M. Gingrich^{30,a},
D. Glenzinski⁹, J. Goldberg²², M.J. Goodrick⁵, W. Gorn⁴, C. Grandi², E. Gross²⁶,
J. Grunhaus²³, M. Gruwé⁸, C. Hajdu³², G.G. Hanson¹², M. Hansroul⁸, M. Hapke¹³,
C.K. Hargrove⁷, P.A. Hart⁹, C. Hartmann³, M. Hauschild⁸, C.M. Hawkes⁵,
R. Hawkings²⁷, R.J. Hemingway⁶, M. Herndon¹⁷, G. Herten¹⁰, R.D. Heuer⁸,
M.D. Hildreth⁸, J.C. Hill⁵, S.J. Hillier¹, P.R. Hobson²⁵, R.J. Homer¹, A.K. Honma^{28,a},
D. Horváth^{32,c}, K.R. Hossain³⁰, R. Howard²⁹, P. Hüntemeyer²⁷, D.E. Hutchcroft⁵,
P. Igo-Kemenes¹¹, D.C. Imrie²⁵, M.R. Ingram¹⁶, K. Ishii²⁴, A. Jawahery¹⁷,
P.W. Jeffreys²⁰, H. Jeremie¹⁸, M. Jimack¹, A. Joly¹⁸, C.R. Jones⁵, G. Jones¹⁶,
M. Jones⁶, U. Jost¹¹, P. Jovanovic¹, T.R. Junk⁸, D. Karlen⁶, V. Kartvelishvili¹⁶,
K. Kawagoe²⁴, T. Kawamoto²⁴, P.I. Kayal³⁰, R.K. Keeler²⁸, R.G. Kellogg¹⁷,
B.W. Kennedy²⁰, J. Kirk²⁹, A. Klier²⁶, S. Kluth⁸, T. Kobayashi²⁴, M. Kobel¹⁰,
D.S. Koetke⁶, T.P. Kokott³, M. Kolrep¹⁰, S. Komamiya²⁴, T. Kress¹¹, P. Krieger⁶,
J. von Krogh¹¹, P. Kyberd¹³, G.D. Lafferty¹⁶, R. Lahmann¹⁷, W.P. Lai¹⁹, D. Lanske¹⁴,
J. Lauber¹⁵, S.R. Lautenschlager³¹, J.G. Layter⁴, D. Lazic²², A.M. Lee³¹, E. Lefebvre¹⁸,
D. Lellouch²⁶, J. Letts¹², L. Levinson²⁶, S.L. Lloyd¹³, F.K. Loebinger¹⁶, G.D. Long²⁸,
M.J. Losty⁷, J. Ludwig¹⁰, A. Macchiolo², A. Macpherson³⁰, M. Mannelli⁸,
S. Marcellini², C. Markus³, A.J. Martin¹³, J.P. Martin¹⁸, G. Martinez¹⁷, T. Mashimo²⁴,
P. Mättig³, W.J. McDonald³⁰, J. McKenna²⁹, E.A. Mckigney¹⁵, T.J. McMahon¹,
R.A. McPherson⁸, F. Meijers⁸, S. Menke³, F.S. Merritt⁹, H. Mes⁷, J. Meyer²⁷,
A. Michelini², G. Mikenberg²⁶, D.J. Miller¹⁵, A. Mincer^{22,e}, R. Mir²⁶, W. Mohr¹⁰,
A. Montanari², T. Mori²⁴, M. Morii²⁴, U. Müller³, S. Mihara²⁴, K. Nagai²⁶,
I. Nakamura²⁴, H.A. Neal⁸, B. Nellen³, R. Nisius⁸, S.W. O'Neale¹, F.G. Oakham⁷,
F. Odorici², H.O. Ogren¹², A. Oh²⁷, N.J. Oldershaw¹⁶, M.J. Oreglia⁹, S. Orito²⁴,

J. Pálinkás^{33,d}, G. Pásztor³², J.R. Pater¹⁶, G.N. Patrick²⁰, J. Patt¹⁰, M.J. Pearce¹,
R. Perez-Ochoa⁸, S. Petzold²⁷, P. Pfeifenschneider¹⁴, J.E. Pilcher⁹, J. Pinfold³⁰,
D.E. Plane⁸, P. Poffenberger²⁸, B. Poli², A. Posthaus³, D.L. Rees¹, D. Rigby¹,
S. Robertson²⁸, S.A. Robins²², N. Rodning³⁰, J.M. Roney²⁸, A. Rooke¹⁵, E. Ros⁸,
A.M. Rossi², P. Routenburg³⁰, Y. Rozen²², K. Runge¹⁰, O. Runolfsson⁸, U. Ruppel¹⁴,
D.R. Rust¹², R. Rylko²⁵, K. Sachs¹⁰, T. Saeki²⁴, E.K.G. Sarkisyan²³, C. Sbarra²⁹,
A.D. Schaile³⁴, O. Schaile³⁴, F. Scharf³, P. Scharff-Hansen⁸, P. Schenk³⁴, J. Schieck¹¹,
P. Schleper¹¹, B. Schmitt⁸, S. Schmitt¹¹, A. Schöning⁸, M. Schröder⁸,
H.C. Schultz-Coulon¹⁰, M. Schumacher³, C. Schwick⁸, W.G. Scott²⁰, T.G. Shears¹⁶,
B.C. Shen⁴, C.H. Shepherd-Themistocleous⁸, P. Sherwood¹⁵, G.P. Siroli², A. Sittler²⁷,
A. Skillman¹⁵, A. Skuja¹⁷, A.M. Smith⁸, G.A. Snow¹⁷, R. Sobie²⁸,
S. Söldner-Rembold¹⁰, R.W. Springer³⁰, M. Sproston²⁰, K. Stephens¹⁶, J. Steuerer²⁷,
B. Stockhausen³, K. Stoll¹⁰, D. Strom¹⁹, P. Szymanski²⁰, R. Tafirout¹⁸, S.D. Talbot¹,
S. Tanaka²⁴, P. Taras¹⁸, S. Tarem²², R. Teuscher⁸, M. Thiergen¹⁰, M.A. Thomson⁸,
E. von Törne³, S. Towers⁶, I. Trigger¹⁸, Z. Trócsányi³³, E. Tsur²³, A.S. Turcot⁹,
M.F. Turner-Watson⁸, P. Utzat¹¹, R. Van Kooten¹², M. Verzocchi¹⁰, P. Vikas¹⁸,
E.H. Vokurka¹⁶, H. Voss³, F. Wäckerle¹⁰, A. Wagner²⁷, C.P. Ward⁵, D.R. Ward⁵,
P.M. Watkins¹, A.T. Watson¹, N.K. Watson¹, P.S. Wells⁸, N. Vermes³, J.S. White²⁸,
B. Wilkens¹⁰, G.W. Wilson²⁷, J.A. Wilson¹, G. Wolf²⁶, T.R. Wyatt¹⁶, S. Yamashita²⁴,
G. Yekutieli²⁶, V. Zacek¹⁸, D. Zer-Zion⁸

¹School of Physics and Space Research, University of Birmingham, Birmingham B15 2TT, UK

²Dipartimento di Fisica dell' Università di Bologna and INFN, I-40126 Bologna, Italy

³Physikalisches Institut, Universität Bonn, D-53115 Bonn, Germany

⁴Department of Physics, University of California, Riverside CA 92521, USA

⁵Cavendish Laboratory, Cambridge CB3 0HE, UK

⁶ Ottawa-Carleton Institute for Physics, Department of Physics, Carleton University, Ottawa, Ontario K1S 5B6, Canada

⁷Centre for Research in Particle Physics, Carleton University, Ottawa, Ontario K1S 5B6, Canada

⁸CERN, European Organisation for Particle Physics, CH-1211 Geneva 23, Switzerland

⁹Enrico Fermi Institute and Department of Physics, University of Chicago, Chicago IL 60637, USA

¹⁰Fakultät für Physik, Albert Ludwigs Universität, D-79104 Freiburg, Germany

¹¹Physikalisches Institut, Universität Heidelberg, D-69120 Heidelberg, Germany

¹²Indiana University, Department of Physics, Swain Hall West 117, Bloomington IN 47405, USA

¹³Queen Mary and Westfield College, University of London, London E1 4NS, UK

¹⁴Technische Hochschule Aachen, III Physikalisches Institut, Sommerfeldstrasse 26-28, D-52056 Aachen, Germany

¹⁵University College London, London WC1E 6BT, UK

¹⁶Department of Physics, Schuster Laboratory, The University, Manchester M13 9PL,

UK

¹⁷Department of Physics, University of Maryland, College Park, MD 20742, USA

¹⁸Laboratoire de Physique Nucléaire, Université de Montréal, Montréal, Quebec H3C 3J7, Canada

¹⁹University of Oregon, Department of Physics, Eugene OR 97403, USA

²⁰Rutherford Appleton Laboratory, Chilton, Didcot, Oxfordshire OX11 0QX, UK

²²Department of Physics, Technion-Israel Institute of Technology, Haifa 32000, Israel

²³Department of Physics and Astronomy, Tel Aviv University, Tel Aviv 69978, Israel

²⁴International Centre for Elementary Particle Physics and Department of Physics, University of Tokyo, Tokyo 113, and Kobe University, Kobe 657, Japan

²⁵Brunel University, Uxbridge, Middlesex UB8 3PH, UK

²⁶Particle Physics Department, Weizmann Institute of Science, Rehovot 76100, Israel

²⁷Universität Hamburg/DESY, II Institut für Experimental Physik, Notkestrasse 85, D-22607 Hamburg, Germany

²⁸University of Victoria, Department of Physics, P O Box 3055, Victoria BC V8W 3P6, Canada

²⁹University of British Columbia, Department of Physics, Vancouver BC V6T 1Z1, Canada

³⁰University of Alberta, Department of Physics, Edmonton AB T6G 2J1, Canada

³¹Duke University, Dept of Physics, Durham, NC 27708-0305, USA

³²Research Institute for Particle and Nuclear Physics, H-1525 Budapest, P O Box 49, Hungary

³³Institute of Nuclear Research, H-4001 Debrecen, P O Box 51, Hungary

³⁴Ludwigs-Maximilians-Universität München, Sektion Physik, Am Coulombwall 1, D-85748 Garching, Germany

^a and at TRIUMF, Vancouver, Canada V6T 2A3

^b and Royal Society University Research Fellow

^c and Institute of Nuclear Research, Debrecen, Hungary

^d and Department of Experimental Physics, Lajos Kossuth University, Debrecen, Hungary

^e and Department of Physics, New York University, NY 1003, USA

1 Introduction

The measurement of the photon structure function F_2^γ , and in particular of its evolution with the momentum transfer squared, Q^2 , is a classic test of perturbative QCD [1]. F_2^γ is expected to increase only logarithmically with Q^2 , therefore the large range of Q^2 values accessible at the e^+e^- collider LEP, which presently extends from about 1 GeV² to about 400 GeV² and which will increase in future, makes it an ideal place to study this evolution.

The results presented in this paper are based on new measurements of F_2^γ using data in the Q^2 range from 6 to 100 GeV² recorded by the OPAL detector in 1996 at $\sqrt{s_{ee}} = 161 - 172$ GeV and on results of the analysis [2, 3] of data collected at e^+e^- centre-of-mass energies $\sqrt{s_{ee}}$ around the mass of the Z^0 (denoted by $\sqrt{s_{ee}} = 91$ GeV). This measurement is an extension of the analysis of F_2^γ detailed in [2] using basically the same methods to analyse the singly-tagged two-photon events at higher $\sqrt{s_{ee}}$.

For singly-tagged events¹ the process $e^+e^- \rightarrow e^+e^- + \textit{hadrons}$ can be regarded as deep inelastic scattering of an e^\pm on a quasi-real photon, where the flux of quasi-real photons can be calculated using the equivalent photon approximation [4]. The cross-section for deep inelastic electron-photon scattering is expressed as [5]:

$$\frac{d^2\sigma_{e\gamma \rightarrow eX}}{dx dQ^2} = \frac{2\pi\alpha^2}{x Q^4} [(1 + (1 - y)^2) F_2^\gamma(x, Q^2) - y^2 F_L^\gamma(x, Q^2)] \quad (1)$$

where $Q^2 = -q^2$ is the negative value of the four-momentum squared of the virtual photon. The usual dimensionless variables of deep inelastic scattering, x and y , are defined as $x = Q^2/2(p \cdot q)$ and $y = (p \cdot q)/(p \cdot k)$, and α is the fine structure constant. The symbols p , q and k denote the four-vectors of the quasi-real photon, the virtual photon and the incoming electron respectively. The structure function F_2^γ is related to the sum over the parton densities of the photon (see e.g. [5]). In the kinematic region of low values of y studied ($y^2 \ll 1$) the contribution of the term proportional to the longitudinal structure function $F_L^\gamma(x, Q^2)$ is negligible.

The paper is organised as follows. After the description of the OPAL detector in section 2 the data selection and background estimates are detailed in section 3. The quality of the description of the observed hadronic final state by the Monte Carlo models is discussed in section 4. The measurement of the evolution of F_2^γ is outlined in section 5. The results are presented in section 6, followed by the conclusions given in section 7.

¹The term singly-tagged denotes the situation where the electron, which radiates the virtual photon, undergoes deep inelastic scattering and is seen (tagged) in the detector, whereas the other electron, which radiates the quasi-real photon, is unseen as it leaves the detector close to the beam direction. In this paper positrons are also referred to as electrons, and the electron and positron masses are neglected.

2 The OPAL detector

The OPAL detector is described in detail elsewhere [6]; only the subdetectors which are most relevant for this analysis, namely the electromagnetic calorimeters and the tracking devices, are detailed below. The OPAL detector has a uniform magnetic field of 0.435 T along the beam direction throughout the central tracking region, with electromagnetic and hadronic calorimetry and muon chambers outside the coil.

In the OPAL right-handed coordinate system the x -axis points towards the centre of the LEP ring, the y -axis points upwards and the z -axis points in the direction of the electron beam. The polar angle θ and the azimuthal angle ϕ are defined with respect to the z -axis and x -axis respectively.

The small-angle silicon tungsten luminometer (SW) covers the region in θ from 25 to 59 mrad. From 1996 onwards, the lower boundary of the acceptance has been increased to 32 mrad following the installation of a low angle shield to protect the central detector against possible synchrotron radiation. The SW consists of two finely segmented calorimeters placed around the beam pipe, one each side of the detector, at a distance of 2.4 m from the interaction point. Each calorimeter is composed of a stack of 19 silicon wafers interleaved with 18 tungsten plates placed perpendicular to the beam axis. The sensitive area of each silicon wafer extends in radius from 62 to 142 mm from the beam axis and is segmented into 32 pads radially and 32 in azimuth around the beam. The radial position of electron showers in the calorimeter can be determined with a typical resolution of 0.06 mrad in θ . The energy resolution for a beam energy electron of 86 GeV energy is approximately 2.5 GeV.

The clean acceptance of the forward detectors (FD) covers the θ region from 60 to 140 mrad at each end of the OPAL detector. The FD consists of cylindrical lead-scintillator calorimeters with a depth of 24 radiation lengths (X_0) divided azimuthally into 16 segments. The energy resolution for electromagnetic showers is $18\%/\sqrt{E}$, where E is in GeV. An array of three planes of proportional tubes buried in the calorimeter at a depth of 4 X_0 provides a precise shower position measurement, with a typical resolution of 3–4 mm, corresponding to 2.5 mrad in θ , and no more than 3.5 mrad in ϕ .

Charged particles are detected by a silicon microvertex detector, a drift chamber vertex detector, and a jet chamber. Outside the jet chamber, but still in the magnetic field, lies a layer of drift chambers whose purpose is to improve the track reconstruction in the z -coordinate. The resolution of the transverse momentum for charged particles is $\sigma_{p_t}/p_t = \sqrt{(0.02)^2 + (0.0015 p_t)^2}$ for $|\cos \theta| < 0.7$, where p_t is in GeV, and degrades for higher values of $|\cos \theta|$.

Both ends of the OPAL detector are equipped with electromagnetic endcap calorimeters covering the range from 200 to 630 mrad in polar angle. They are homogeneous devices composed of arrays of lead-glass blocks of 9.2×9.2 cm² cross-section and typ-

ically $22 X_0$ in depth, giving good shower containment. In the central region, outside the solenoid, is the electromagnetic barrel calorimeter of similar construction.

The deep inelastic scattering events are triggered with high efficiency by the large energy deposits of the scattered electron in the calorimeters and by charged particle tracks seen in the tracking devices.

3 Kinematics and data selection

The measurement of $F_2^\gamma(x, Q^2)$ requires the determination of x and Q^2 which are obtained from the four-vectors of the tagged electron and the hadronic final state as follows:

$$Q^2 = 2 E_b E_{\text{tag}} (1 - \cos \theta_{\text{tag}}) \quad (2)$$

$$x = \frac{Q^2}{Q^2 + W^2 + P^2} \quad (3)$$

Here E_{tag} and θ_{tag} are the energy and polar angle of the tagged electron, E_b is the beam energy, and W the invariant mass of the hadronic final state. $P^2 = -p^2$ is the negative value of the virtuality of the quasi-real photon. For this singly-tagged sample, an antitag condition on the second electron is applied (see list of cuts below). This ensures that P^2 is much smaller than Q^2 and it is therefore neglected in the evaluation of x using Eq. 3.

The four-momentum of the hadronic system is calculated by summing over all charged particle tracks (assuming the pion mass) and calorimeter clusters, where quality criteria are applied to both the tracks and the clusters to ensure that they are well reconstructed. To avoid double counting of particle momenta, a matching algorithm for the association of a charged particle track with a cluster is applied [7].

The analysis uses the data at $\sqrt{s_{ee}} = 161 - 172$ GeV with an integrated e^+e^- luminosity of 18.1 ± 0.1 pb $^{-1}$, as determined from small-angle Bhabha scattering events. The tagged electron is detected either in the SW detectors ($Q^2 \approx 6 - 20$ GeV 2) or in the FD detectors ($Q^2 \approx 20 - 100$ GeV 2). These two samples are subject to slightly different selection criteria and are referred to as the SW and FD samples. Candidate events for the process $\gamma^*\gamma \rightarrow \text{hadrons}$ are required to satisfy criteria for the tagged electron as well as for the hadronic final state, in addition to several technical cuts, to ensure good detector status and track quality. The event selection listed below is designed to have a high efficiency for signal events and to reject background events, which mainly stem from the process $\gamma^*\gamma \rightarrow \tau^+\tau^-$. The requirements for the SW (FD) samples are:

1. A tagged electron candidate is required to produce a cluster in a SW (FD) detector with an energy of $E_{\text{tag}} \geq 0.775 E_b$ ($E_{\text{tag}} \geq 0.60 E_b$) and a polar angle

of $33 \leq \theta_{\text{tag}} \leq 55$ ($60 \leq \theta_{\text{tag}} \leq 120$) mrad with respect to either of the beam directions.

2. The energy E_{at} of the most energetic cluster in the hemisphere opposite to the one which contains the tagged electron is restricted to $E_{\text{at}} \leq 0.08 E_b$ (antitag requirement).
3. There must be at least three tracks originating from the hadronic final state, $N_{\text{ch}} \geq 3$.
4. The visible invariant mass W_{vis} of the hadronic system, calculated as the mass of the four-momentum vector of the hadronic system as defined above, is required to be in the range $2.5 \leq W_{\text{vis}} \leq 40$ GeV.

The harder requirement on the tag energy applied to events of the SW sample reflects the much higher background from off-momentum electrons closer to the beam direction. An off-momentum electron is an electron that was lost from the beam and scattered into the detector. In addition to the off-momentum electron, due to an interaction that occurs close to the nominal interaction point, charged particles are produced which fulfill the requirements for the hadronic final state. Since the energy spectrum of the off-momentum electrons peaks around $0.5E_b$, this background is essentially eliminated by requiring $E_{\text{tag}} \geq 0.775 E_b$.

With these cuts 879 and 414 events with average squared momentum transfers $\langle Q^2 \rangle$ of approximately 11 GeV² and 41 GeV², are selected in the SW and FD samples respectively. The accessible x range for the two samples is $0.004 < x < 0.76$ and $0.012 < x < 0.94$ respectively. The trigger efficiency is evaluated from the data to be above 98% for the SW sample and essentially 100% for the FD sample.

The background to the $\gamma^*\gamma \rightarrow \text{hadrons}$ signal comes from events which contain a true or fake tagged electron and an apparent low-mass hadronic final state (compared to $\sqrt{s_{ee}}$). The dominant source of this background is $\gamma^*\gamma \rightarrow \text{leptons}$ and particularly $\gamma^*\gamma \rightarrow \tau^+\tau^-$. These processes were simulated with the Vermaseren program [8]. The background contribution from $\gamma^*\gamma \rightarrow \tau^+\tau^-$ events is 36.0 ± 1.8 (29.0 ± 2.2) events and the $\gamma^*\gamma \rightarrow e^+e^-$ process contributes 16.8 ± 1.2 (9.1 ± 0.9) events to the SW (FD) samples respectively. Additional background sources like $Z^0 \rightarrow \text{hadrons}$ events, four-fermion events with $e^+e^- q\bar{q}$ and $e^+e^- \ell^+\ell^-$ ($\ell = e, \mu, \tau$) final states, and $Z^0 \rightarrow \tau^+\tau^-$ events, were studied. The total contribution of these processes to the background is of the order of 1 and 3 events in the two samples, respectively, and consequently they are neglected.

Events with a scattered electron observed in the electromagnetic endcap calorimeter allow higher values of Q^2 to be reached than in the SW and FD samples. With the current level of integrated luminosity collected at $\sqrt{s_{ee}} = 161 - 172$ GeV too few such events have been observed to allow a detailed analysis to be performed.

4 Description of the hadronic final state

The measurement of F_2^γ requires the determination of W from the hadronic final state. Because of the finite detector resolution and the incomplete angular coverage, especially in the forward region, the correlation between visible hadronic mass, W_{vis} , and W depends critically on the modelling of the hadronic final state, which is correlated with the observed hadronic energy flow. Therefore a detailed comparison of the observed hadronic final state and the predictions from the various Monte Carlo models is needed. The results of this study, which follows closely the one described in [2], are summarised in this section.

The set of Monte Carlo generators used to simulate the signal events differs only slightly from that used in the previous analysis [2]. HERWIG [9] version 5.9 is used instead of 5.8d with the charm quark mass altered from 1.8 GeV to 1.55 GeV. All events are generated without the simulation of the soft underlying event [2]. The F2GEN [10] generator is used to simulate events based on F_2^γ for four flavours (u,d,s,c) with $m_c = 1.5$ GeV, rather than with three flavours and with the charm contribution added using the Vermaseren program, as in [2]. The PYTHIA [11] Monte Carlo remains the same as in [2]. The integrated luminosity of each Monte Carlo sample corresponds to approximately ten times the integrated luminosity of the data. The Monte Carlo generation was based either on the leading order (LO) GRV [12] or the LO SaS1D [13] parton density parametrisations. All Monte Carlo events are passed through the OPAL detector simulation program [14] and the same reconstruction and analysis chain as the real data events.

For the comparison of the observed hadronic final states to the Monte Carlo predictions a particle is defined as a track or a cluster resulting from the matching algorithm [7]. In [2] it was shown that none of the models used accurately described the angular distribution and the transverse energy of the hadronic final state. These discrepancies persist at higher centre-of-mass energies. The accessible Q^2 region for the SW sample is similar to that of the low- Q^2 sample of the analysis at $\sqrt{s_{ee}} = 91$ GeV [2], where the scattered electron was observed in the FD.

Figure 1 shows the hadronic energy flow per event, $1/N \text{ d}E/\text{d}\eta$, as a function of pseudorapidity, $\eta = -\ln(\tan(\theta'/2))$, for the SW sample and the FD sample for two bins in x_{vis} . Only statistical errors are shown. The tagged electron is always at negative pseudorapidity and is not shown. In the region $0.1 < x_{\text{vis}} < 0.6$ the agreement between data and the various models is satisfactory, with the exception of the region $-4 < \eta < -2$ for the SW sample where all Monte Carlos are low compared to the data. This effect comes from leakage into the FD detector and is almost entirely eliminated if the requirement for the maximum θ_{tag} for the SW sample is restricted to smaller angles. This is taken into account in the evaluation of the systematic error on F_2^γ . Significant differences are observed for $x_{\text{vis}} < 0.1$. In the remnant direction at positive η , both HERWIG and PYTHIA tend to overestimate the energy deposited in the forward region of the detector. In the central region, however, they underestimate

the transverse energy. In contrast, the pointlike events generated with the F2GEN model lie higher than the data in the central region and lower in the forward region. The number of events with $x_{\text{vis}} > 0.6$ is insufficient to allow firm conclusions to be drawn.

The minimum tag energy and the antitag requirement for the FD sample of this analysis are slightly different from the ones used for the low- Q^2 sample in [2]. This results in a different shape of the energy flow distributions and a slightly improved quality of the data description by the Monte Carlo models.

In summary, in the intermediate range of x_{vis} a good overall agreement between the data and the Monte Carlo models is found for both samples. At $x_{\text{vis}} < 0.1$ the flow of hadronic energy into the central region of the detector is underestimated by the HERWIG and PYTHIA Monte Carlo models, and overestimated by the F2GEN model. Improved Monte Carlo models would be therefore required in order to reduce the model-dependent systematic errors on the measurement of F_2^γ in this region.

5 Determination of F_2^γ

To obtain the photon structure function F_2^γ in bins of Q^2 from the measured x_{vis} distribution the method of regularised unfolding is employed [15]. In this method, a reference Monte Carlo is used to obtain the detector efficiency and resolution and the regularisation reduces the effect of inherent oscillating fluctuations of the unfolded structure function. See [2] for more details of this procedure. To unfold F_2^γ from the data HERWIG, with the F_2^γ structure function based on the GRV parametrisation, is chosen as the reference Monte Carlo. This choice is motivated by the fact that HERWIG gives a slightly better description of the hadronic final state than PYTHIA, (see [2] and Fig. 1). The reference Monte Carlo is used to determine the central values and most of the systematic uncertainties. The PYTHIA and the F2GEN models are used to estimate the model dependence of the result.

The data at $\sqrt{s_{\text{ee}}} = 161 - 172$ GeV are subdivided into four Q^2 ranges, two ranges for the SW sample and two for the FD sample. The ranges in Q^2 are 6–11, 11–20, 20–40 and 40–100 GeV² with average squared momentum transfers of $\langle Q^2 \rangle = 9, 14.5, 30$ and 59 GeV² respectively. The x_{vis} distributions of the SW and FD samples are shown in Figs. 2a and 2b. The distributions of the reference Monte Carlo with background added are shown by the dashed histograms. In addition, the background events are shown separately at the bottom of the figure. The number of Monte Carlo events is the absolute prediction for the data luminosity. The solid histogram represents the reweighted distribution of the signal Monte Carlo with background added after the unfolding has been performed [2]. From the figures one observes that the mean x_{vis} increases with increasing Q^2 , and that the x_{vis} distribution of the data is well represented by the sum of the reweighted signal Monte Carlo and background Monte

Carlo samples after unfolding.

The weight factors for each individual event, obtained from the unfolding, can be used to construct reweighted Monte Carlo distributions of different variables. The reweighted distributions are the Monte Carlo predictions based on the structure function unfolded from the data. Any reweighting based on the generated x distribution will change the shape of other measurable variables besides x_{vis} . As all variables are differently correlated with x_{vis} the comparison of their distributions with the data gives an important check of the transformation, as described by the Monte Carlo simulation, between the partonic distributions and the measurable distributions. As an example Figs. 2c and 2d show the Q^2 distributions of the SW and FD samples, applying the cuts listed in Sect. 3. There is good agreement in the shape of the distributions. The distributions from both Monte Carlo samples differ slightly in normalisation from the distributions observed in the data, and the agreement improves after the reweighting based on the unfolding of the x_{vis} distribution. A similar behaviour is found for other observables, both for quantities measured from the electron, like E_{tag} and θ_{tag} , and for distributions obtained from the hadronic final state, like N_{ch} and W_{vis} .

6 Results

The unfolded F_2^γ measurements for the data taken at $\sqrt{s_{\text{ee}}} = 161 - 172$ GeV are shown in Figs. 3a–3f, and are listed in Table 1. The value of F_2^γ/α is shown at the centre of the x bin. The bin sizes are indicated by the vertical lines at the top of the figure. The error bars show both the statistical error alone and the full error, given by the quadratic sum of statistical and systematic errors. The central values and statistical errors of the F_2^γ measurements are estimated by using the reference unfolding. The F_2^γ values presented here are not corrected for the fact that P^2 is not strictly equal to zero [2].

The estimation of the systematic error includes three parts [2]: the variation of the compositions of signal and background events in the sample, the use of different F_2^γ structure functions assumed in the Monte Carlo samples, and the different modelling of the formation of the hadronic final state. To allow for a different composition of signal and background events, the event selection cuts are varied. The choice of the cut variations reflects the different population of signal events in the four Q^2 ranges, in terms of the scattering angle of the electron and W_{vis} , as well as the different behaviour of the background events. In each case the unfolding is carried out using the reference Monte Carlo model where only one cut is varied from the standard set. To study the uncertainty due to the structure functions assumed in the Monte Carlo samples, for the SW sample, the unfolding is done using the HERWIG generator, the standard set of cuts and the SaS1D parton density parametrisations. The effect of the different modelling of the formation of the hadronic final state is studied by repeating the unfolding using the PYTHIA Monte Carlo model with the SaS1D parametrisation,

and the F2GEN Monte Carlo model with the GRV parametrisation. The systematic error assigned to the result, shown in Table 1, is taken as the maximum deviation of any unfolding result from the central values, which in some cases leads to rather asymmetric errors, particularly when the HERWIG Monte Carlo model is replaced by PYTHIA or F2GEN. The systematic error is dominated by the model uncertainties.

The measured F_2^γ as function of x is almost flat within the region studied and the absolute normalisation of F_2^γ is well described by various predictions. Shown in Fig. 3 are the F_2^γ predictions for the leading order GRV and the SaS1D parton density parametrisations evaluated at the corresponding values of $\langle Q^2 \rangle$. In each case the expected contribution from massive charm quarks is added. The fact that the charm threshold depends on x and varies with Q^2 causes the change in shape of the predictions, see Eq. 3 for $W = 2m_c$. Both parametrisations successfully describe the measured F_2^γ as a function of x in all Q^2 ranges.

Figure 3 also shows an augmented asymptotic prediction for F_2^γ . The contribution to F_2^γ from the three light flavours is approximated by Witten's leading order asymptotic form [1], using the parametrisation given in [16]. This has been augmented by adding a charm contribution evaluated from the Bethe-Heitler formula [17], and an estimate of the hadronic part of the photon structure function, which essentially corresponds to the hadronic part of the GRV (LO) parametrisation of F_2^γ . The hadronic contribution is derived from the structure function parametrisation of the pion [18] using VDM arguments as detailed in [19] and evolved to the corresponding values of $\langle Q^2 \rangle$. The components are evaluated in leading order using $\Lambda_3^{\overline{\text{MS}}} = 0.232$ GeV. It is known [19, 20] that the asymptotic solution, which is obtained by neglecting terms in the evolution equations that vanish for $Q^2 \rightarrow \infty$, has deficits in the region of low x , because the remaining terms create divergences in the solution which do not occur in the solution of the full evolution equations [19]. However, the asymptotic solution has the appealing feature that it is calculable in QCD, even at higher order [21] and for medium x and with increasing Q^2 it should be more reliable. In addition at high x and Q^2 the hadronic contribution is expected to be small. In the region of medium x values studied here this asymptotic prediction in general lies higher than the GRV and SaS predictions but it is still in agreement with the data. The importance of the hadronic contribution to F_2^γ , which is shown separately at the bottom of the figure, decreases with increasing x and Q^2 , and it accounts for only 15% of F_2^γ at $Q^2 = 59$ GeV² and $x = 0.5$. The asymptotic solution increases with decreasing $\Lambda_3^{\overline{\text{MS}}}$. For $Q^2 = 59$ GeV² and $x = 0.5$ the change in F_2^γ is +24% and -16% if $\Lambda_3^{\overline{\text{MS}}}$ is changed from $\Lambda_3^{\overline{\text{MS}}} = 0.232$ GeV to 0.1 GeV and 0.4 GeV respectively.

As in the previous analysis, F_2^γ/α is also determined in bins of Q^2 in the region $0.1 < x < 0.6$. The new results, together with the result of the previous analysis [2], are shown as a function of Q^2 in Fig. 4a and listed in Table 2. For the results based on the data taken at $\sqrt{s_{ee}} = 161 - 172$ GeV the systematic error is evaluated as described above. The results of the two analyses at very different centre-of-mass energies, using different detector components to detect the scattered electron for similar Q^2 values, are found to

be consistent. An increase of F_2^γ/α with Q^2 is observed in the data, in agreement with the QCD predictions and with results obtained by other experiments [22]. The data are compared to the LO predictions of the GRV and the SaS1D parametrisations, both including the contribution to F_2^γ from massive charm quarks, and to a higher order (HO) calculation [23] based on the HO GRV parametrisation for three light quarks, complemented by the contribution of charm quarks to F_2^γ based on the HO calculation using massive charm quarks of [24], as described in more detail in [2]. The differences between the three predictions are small compared to the experimental errors, and all predictions nicely agree with the data.

In addition the data are compared to the asymptotic prediction as detailed above. This approximation lies higher than the data at low Q^2 and approaches the data at the highest Q^2 reached.

The evolution of F_2^γ with Q^2 is measured by fitting a linear function of the form $a + b \ln(Q^2/\text{GeV}^2)$ to the four data points obtained at $\sqrt{s_{ee}} = 161 - 172$ GeV. Here a and b are parameters which do not depend on x . The result is

$$F_2^\gamma(Q^2)/\alpha = (0.24 \pm 0.11_{-0.18}^{+0.06}) + (0.06 \pm 0.04_{-0.02}^{+0.05}) \ln(Q^2/\text{GeV}^2).$$

The central values and statistical errors of the two parameters are obtained by a fit to the central values of the individual points listed in Table 2 using their statistical errors. The quality of the fit is satisfactory with $\chi^2/\text{dof} = 0.33$ for the central value. The systematic errors are obtained from the maximum deviation from the central values to either side observed when repeating the fit for all variations of cuts, structure functions assumed in the Monte Carlo and Monte Carlo models as discussed above. This procedure automatically takes into account the correlation of the systematic uncertainties between the individual points.

This measurement is consistent with the result of the previous analysis [2] which used the data sample at $\sqrt{s_{ee}} = 91$ GeV in the Q^2 range 7.5–135 GeV², and which was based on a slightly different fitting procedure. A combined fit to the OPAL data at $\sqrt{s_{ee}} = 91$ GeV and 161 – 172 GeV in the Q^2 range of 7.5–135 GeV² yields:

$$F_2^\gamma(Q^2)/\alpha = (0.16 \pm 0.05_{-0.16}^{+0.17}) + (0.10 \pm 0.02_{-0.02}^{+0.05}) \ln(Q^2/\text{GeV}^2)$$

with $\chi^2/\text{dof} = 0.77$ for the central value. The slope $\alpha^{-1}dF_2^\gamma/d \ln Q^2$ is significantly different from zero and the error is somewhat reduced compared to [2] due to the inclusion of the data at higher centre-of-mass energies.

The QCD prediction for the scaling violation behaviour of F_2^γ is different from the proton case. With increasing Q^2 , the proton structure function, F_2^p , increases at small x and decreases at large x , ($x \gtrsim 0.1$). In contrast, due to the pointlike coupling of the photon to quarks, the photon structure function F_2^γ is expected to increase with Q^2 for all values of x , and the size of the scaling violation is expected to depend on x . To examine whether the data exhibit the predicted variation in $\alpha^{-1}dF_2^\gamma/d \ln Q^2$, the Q^2 range 1.86–135 GeV² is analysed using common x ranges, as listed in Table 3.

The published results are rebinned in x but not reanalysed, i.e. the systematic error is evaluated as described in [2, 3].

Figure 4b shows the measurement in comparison to the HO calculation. The points of inflection of F_2^γ for Q^2 below 15 GeV² are caused by the charm threshold. The predictions are in agreement with the observed evolution of F_2^γ with Q^2 in all ranges of x . In order to observe experimentally the variation of $\alpha^{-1}dF_2^\gamma/d\ln Q^2$ with x more data and a reduction of the systematic error are needed.

7 Summary and conclusions

The complete data samples taken by the OPAL experiment at LEP at $\sqrt{s_{ee}} = 91$ GeV and $\sqrt{s_{ee}} = 161 - 172$ GeV have been used to study the hadronic structure of the photon.

A slightly better agreement between the predictions for the hadronic energy flow of the various models and the data in the region $0.1 < x_{\text{vis}} < 0.6$ is found for the data taken at $\sqrt{s_{ee}} = 161 - 172$ GeV than for the data collected at $\sqrt{s_{ee}} = 91$ GeV. At $x_{\text{vis}} < 0.1$ significant differences persist, as the data prefer a more pointlike hadronic energy flow than assumed in either HERWIG or PYTHIA, and at $x_{\text{vis}} > 0.6$ the statistical precision is insufficient to draw firm conclusions.

Using the OPAL data at $\sqrt{s_{ee}} = 161 - 172$ GeV the photon structure function $F_2^\gamma(x, Q^2)$ has been unfolded as a function of x in four Q^2 intervals, with mean momentum transfers $\langle Q^2 \rangle = 9, 14.5, 30$ and 59 GeV². Combining the OPAL data at $\sqrt{s_{ee}} = 91$ GeV and $161 - 172$ GeV, the evolution of F_2^γ with Q^2 in the range $0.10 < x < 0.60$ has been measured to be $F_2^\gamma(Q^2)/\alpha = (0.16 \pm 0.05_{-0.16}^{+0.17}) + (0.10 \pm 0.02_{-0.02}^{+0.05}) \ln(Q^2/\text{GeV}^2)$, where the first error is statistical and the second systematic. From the OPAL data alone the slope $\alpha^{-1}dF_2^\gamma/d\ln Q^2$ is found to be significantly different from zero and consistent with the logarithmic evolution of F_2^γ with Q^2 expected from QCD. The dependence of the scaling violation of F_2^γ on x was studied in three ranges in x , $0.02 - 0.10$, $0.10 - 0.25$ and $0.25 - 0.60$. The QCD prediction was found to be in agreement with the data, but the accuracy of the data is insufficient to show a significantly different slope of F_2^γ for the three ranges in x studied. The precision of the measurement of the logarithmic slope of F_2^γ is primarily limited by systematic errors due to the modelling of the hadronic final state, not by the experimental statistics. There would be scope for considerable improvements if the Monte Carlo models could be improved to represent all aspects of the data.

The data, over the x and Q^2 range studied, are equally well described by several of the available parton density parametrisations, including the GRV and SaS1D parametrisations used in this analysis. They are also satisfactorily described by an F_2^γ based on the asymptotic solution in leading order for three light flavours augmented

by the Bethe-Heitler contribution of charm quarks and a leading order hadronic part based on VDM.

Acknowledgements

We thank E. Laenen for providing the higher order calculations for the evolution of the structure function and E. Laenen and A. Vogt for valuable discussions.

We particularly wish to thank the SL Division for the efficient operation of the LEP accelerator at all energies and for their continuing close cooperation with our experimental group. We thank our colleagues from CEA, DAPNIA/SPP, CE-Saclay for their efforts over the years on the time-of-flight and trigger systems which we continue to use. In addition to the support staff at our own institutions we are pleased to acknowledge the

Department of Energy, USA,
National Science Foundation, USA,
Particle Physics and Astronomy Research Council, UK,
Natural Sciences and Engineering Research Council, Canada,
Israel Science Foundation, administered by the Israel Academy of Science and Humanities,
Minerva Gesellschaft,
Benozio Center for High Energy Physics,
Japanese Ministry of Education, Science and Culture (the Monbusho) and a grant under the Monbusho International Science Research Program,
German Israeli Bi-national Science Foundation (GIF),
Bundesministerium für Bildung, Wissenschaft, Forschung und Technologie, Germany,
National Research Council of Canada,
Hungarian Foundation for Scientific Research, OTKA T-016660, T023793 and OTKA F-023259.

References

- [1] E. Witten, Nucl. Phys. B120 (1977) 189.
- [2] OPAL Collaboration, K. Ackerstaff et al., Z. Phys. C74 (1997) 33.
- [3] OPAL Collaboration, K. Ackerstaff et al., CERN-PPE/97-103, submitted to Phys. Lett. B.
- [4] C. F. von Weizsäcker, Z. Phys. 88 (1934) 612;
E. J. Williams, Phys. Rev. 45 (1934) 729;

- V. M. Budnev, I. F. Ginzburg, G. V. Meledin and V. G. Serbo, Phys. Rep. 15 (1975) 181.
- [5] C. Berger and W. Wagner, Phys. Rep. 146 (1987) 1.
- [6] OPAL Collaboration, K. Ahmet et al., Nucl. Instrum. Meth. A305 (1991) 275;
P. P. Allport et al., Nucl. Instr. and Meth. A324 (1993) 34;
P. P. Allport et al., Nucl. Instr. and Meth. A346 (1994) 476;
B. E. Anderson et al., IEEE Transactions on Nuclear Science 41 (1994) 845.
- [7] OPAL Collaboration, G. Alexander et al., Phys. Lett. B377 (1996) 181.
- [8] J. Smith, J. A. M. Vermaseren and G. Grammer Jr, Phys. Rev. D15 (1977) 3280;
R. Bhattacharya, G. Grammer Jr and J. Smith, Phys. Rev. D15 (1977) 3267;
J. A. M. Vermaseren, J. Smith and G. Grammer Jr, Phys. Rev. D19 (1979) 137;
J. A. M. Vermaseren, Nucl. Phys. B229 (1983) 347.
- [9] G. Marchesini et al., Comp. Phys. Comm. 67 (1992) 465.
- [10] A. Buijs, W. G. J. Langeveld, M. H. Lehto and D. J. Miller, Comp. Phys. Comm. 79 (1994) 523.
- [11] T. Sjöstrand, Comp. Phys. Comm. 82 (1994) 74;
T. Sjöstrand, PYTHIA 5.7 and JETSET 7.4, Physics and Manual, CERN-TH/93-7112 (1993).
- [12] M. Glück, E. Reya and A. Vogt, Phys. Rev. D45 (1992) 3986;
M. Glück, E. Reya and A. Vogt, Phys. Rev. D46 (1992) 1973.
- [13] G. A. Schuler and T. Sjöstrand, Z. Phys. C68 (1995) 607.
- [14] J. Allison et al., Nucl. Instr. and Meth. A317 (1992) 47.
- [15] V. Blobel, DESY84-118 (1984);
V. Blobel, RUN program manual, unpublished (1996).
- [16] L. E. Gordon and J. K. Storrow, Z. Phys. C56 (1992) 307.
- [17] E. Witten, Nucl. Phys. B104 (1976) 445.
- [18] M. Glück, E. Reya and A. Vogt, Z. Phys. C53 (1992) 651.
- [19] M. Glück, K. Grassie and E. Reya, Phys. Rev. D30 (1984) 1447.
- [20] M. Glück and E. Reya, Phys. Rev. D28 (1983) 2749.
- [21] W. A. Bardeen and A. J. Buras, Phys. Rev. D20 (1979) 166.

- [22] TPC/ 2γ Collaboration, H. Aihara et al., Z. Phys. C34 (1987) 1;
TPC/ 2γ Collaboration, H. Aihara et al., Phys. Rev. Lett. 58 (1987) 97;
DELPHI Collaboration, P. Abreu et al., Z. Phys. C69 (1996) 223;
JADE Collaboration, W. Bartel et al., Z. Phys. C24 (1984) 231;
TOPAZ Collaboration, K. Muramatsu et al., Phys. Lett. B332 (1994) 477.
- [23] E. Laenen, private communication.
- [24] E. Laenen, J. Smith, S. Riemersma and W. L. van Neerven, Phys. Rev. D49 (1994) 5753.

Q^2 range [GeV ²]	$\langle Q^2 \rangle$ [GeV ²]	Δx	F_2^γ/α
6–11	9	0.020 – 0.100	$0.33 \pm 0.03^{+0.06}_{-0.06}$
		0.100 – 0.250	$0.29 \pm 0.04^{+0.04}_{-0.05}$
		0.250 – 0.600	$0.39 \pm 0.08^{+0.30}_{-0.10}$
11–20	14.5	0.020 – 0.100	$0.37 \pm 0.03^{+0.16}_{-0.01}$
		0.100 – 0.250	$0.42 \pm 0.05^{+0.04}_{-0.14}$
		0.250 – 0.600	$0.39 \pm 0.06^{+0.10}_{-0.11}$
20–40	30	0.050 – 0.100	$0.32 \pm 0.04^{+0.11}_{-0.02}$
		0.100 – 0.350	$0.52 \pm 0.05^{+0.06}_{-0.13}$
		0.350 – 0.600	$0.41 \pm 0.09^{+0.20}_{-0.05}$
		0.600 – 0.800	$0.46 \pm 0.15^{+0.39}_{-0.14}$
40–100	59	0.050 – 0.100	$0.37 \pm 0.06^{+0.28}_{-0.07}$
		0.100 – 0.350	$0.44 \pm 0.07^{+0.08}_{-0.07}$
		0.350 – 0.600	$0.48 \pm 0.09^{+0.16}_{-0.10}$
		0.600 – 0.800	$0.51 \pm 0.14^{+0.48}_{-0.02}$
6–20	11	0.020 – 0.100	$0.34 \pm 0.02^{+0.11}_{-0.02}$
		0.100 – 0.250	$0.36 \pm 0.03^{+0.02}_{-0.10}$
		0.250 – 0.600	$0.39 \pm 0.04^{+0.12}_{-0.04}$
20–100	41	0.050 – 0.100	$0.33 \pm 0.03^{+0.15}_{-0.03}$
		0.100 – 0.350	$0.49 \pm 0.04^{+0.02}_{-0.12}$
		0.350 – 0.600	$0.43 \pm 0.07^{+0.15}_{-0.05}$
		0.600 – 0.800	$0.54 \pm 0.11^{+0.41}_{-0.11}$

Table 1: Results for F_2^γ as a function of x for four active flavours in bins of Q^2 for the data taken at $\sqrt{s_{ee}} = 161 - 172$ GeV. The first errors are statistical and the second systematic. The SW sample with $\langle Q^2 \rangle = 11$ GeV² consists of the data from $\langle Q^2 \rangle = 9$ and 14.5 GeV² and the FD sample with $\langle Q^2 \rangle = 41$ GeV² consists of the data from $\langle Q^2 \rangle = 30$ and 59 GeV².

$\langle Q^2 \rangle$	F_2^γ/α	Ref.
7.5	$0.36 \pm 0.02^{+0.06}_{-0.12}$	[2]
14.7	$0.41 \pm 0.01^{+0.08}_{-0.04}$	[2]
135	$0.71 \pm 0.07^{+0.14}_{-0.05}$	[2]
9	$0.36 \pm 0.05^{+0.08}_{-0.06}$	
14.5	$0.41 \pm 0.04^{+0.04}_{-0.11}$	
30	$0.48 \pm 0.05^{+0.06}_{-0.07}$	
59	$0.46 \pm 0.06^{+0.07}_{-0.04}$	
11	$0.38 \pm 0.03^{+0.06}_{-0.03}$	
41	$0.47 \pm 0.04^{+0.06}_{-0.03}$	

Table 2: Results for F_2^γ for four active flavours in bins of Q^2 for $0.10 < x < 0.60$. The first errors are statistical and the second systematic. The bins in Q^2 for the analysis of the data taken at $\sqrt{s_{ee}} = 161 - 172$ GeV are defined in Table 1. The SW sample with $\langle Q^2 \rangle = 11$ GeV² consists of the data from $\langle Q^2 \rangle = 9$ and 14.5 GeV² and the FD sample with $\langle Q^2 \rangle = 41$ GeV² consists of the data from $\langle Q^2 \rangle = 30$ and 59 GeV². The combined results at $\langle Q^2 \rangle = 11$ and 41 GeV² are shown for completeness and are not used in the fit of the slope of F_2^γ , Fig. 4a.

Δx	0.02 – 0.10	0.10 – 0.25	0.25 – 0.60	Ref.
$\langle Q^2 \rangle$	F_2^γ/α	F_2^γ/α	F_2^γ/α	
1.86	$0.22 \pm 0.01^{+0.06}_{-0.04}$	–	–	[3]
3.76	$0.30 \pm 0.01^{+0.06}_{-0.03}$	$0.32 \pm 0.02^{+0.10}_{-0.03}$	–	[3]
7.5	$0.27 \pm 0.02^{+0.02}_{-0.06}$	$0.32 \pm 0.02^{+0.08}_{-0.14}$	$0.38 \pm 0.04^{+0.05}_{-0.18}$	[2]
14.7	$0.37 \pm 0.01^{+0.05}_{-0.15}$	$0.40 \pm 0.02^{+0.06}_{-0.04}$	$0.42 \pm 0.02^{+0.09}_{-0.09}$	[2]
135	–	$0.62 \pm 0.09^{+0.12}_{-0.05}$	$0.73 \pm 0.07^{+0.04}_{-0.05}$	[2]
11	$0.34 \pm 0.02^{+0.11}_{-0.02}$	$0.36 \pm 0.03^{+0.02}_{-0.10}$	$0.39 \pm 0.04^{+0.12}_{-0.04}$	
41	$0.32 \pm 0.03^{+0.19}_{-0.03}$	$0.46 \pm 0.04^{+0.02}_{-0.13}$	$0.46 \pm 0.05^{+0.10}_{-0.06}$	

Table 3: Results for F_2^γ for four active flavours in bins of Q^2 and x . The first errors are statistical and the second systematic. The bins in Q^2 for the analysis of the data taken at $\sqrt{s_{ee}} = 161 - 172$ GeV are defined in Table 1. The results from [2, 3] are rebinned to match the same ranges in x . For statistical reasons only the combined samples with $\langle Q^2 \rangle = 11$ and 41 GeV² are used for the subdivision into several bins in x , Fig. 4b.

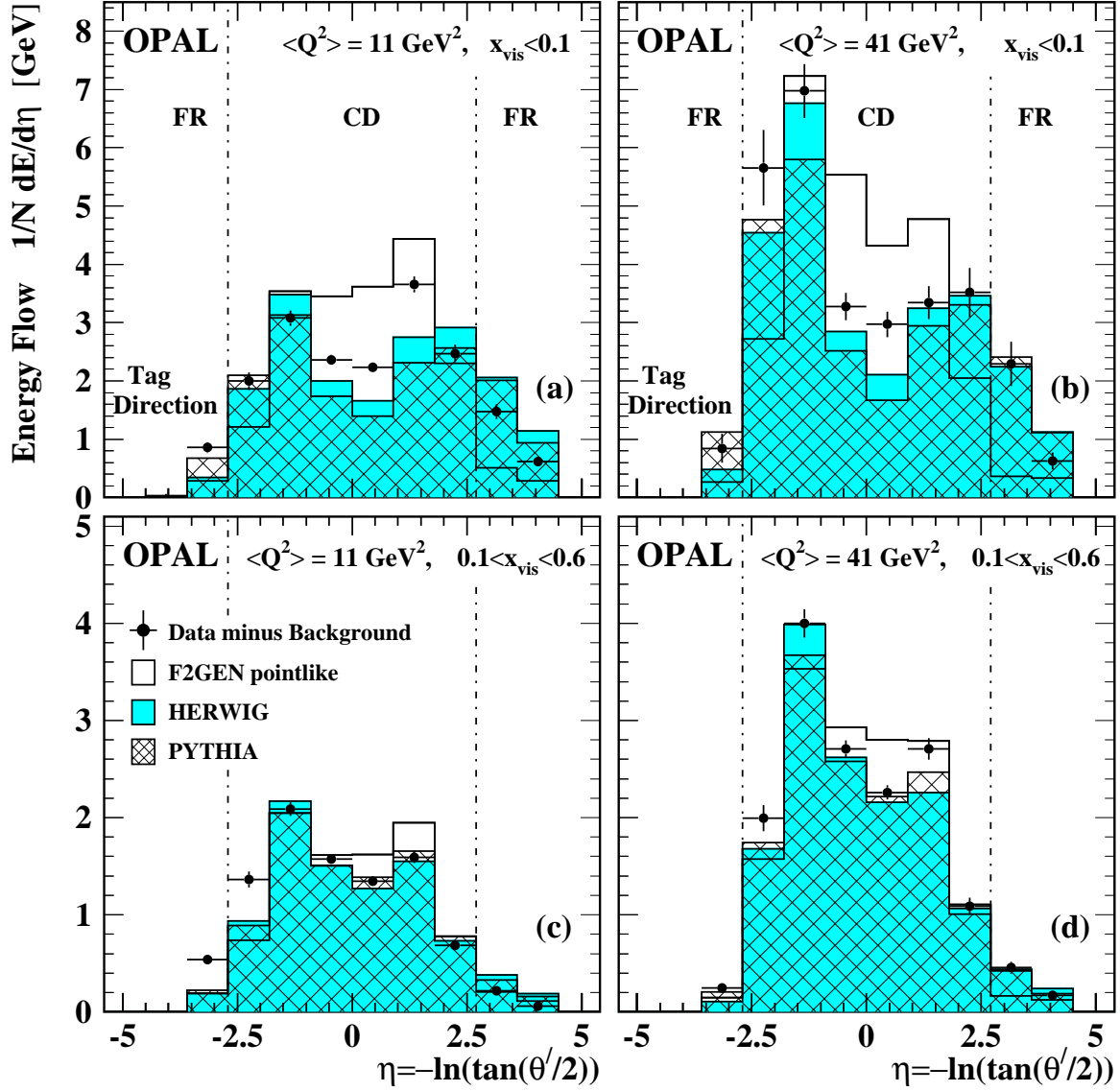


Figure 1: The hadronic energy flow per event as a function of pseudorapidity η for the data taken at $\sqrt{s_{ee}} = 161 - 172 \text{ GeV}$ and various signal Monte Carlo samples. The energy flow is shown for two ranges of x_{vis} for the SW and FD samples. The errors shown are statistical only. The tagged electron is always at negative pseudorapidity and is not shown. The different regions in rapidity indicated denote the forward region (FR) which contains the SW and FD detectors and the central detector (CD).

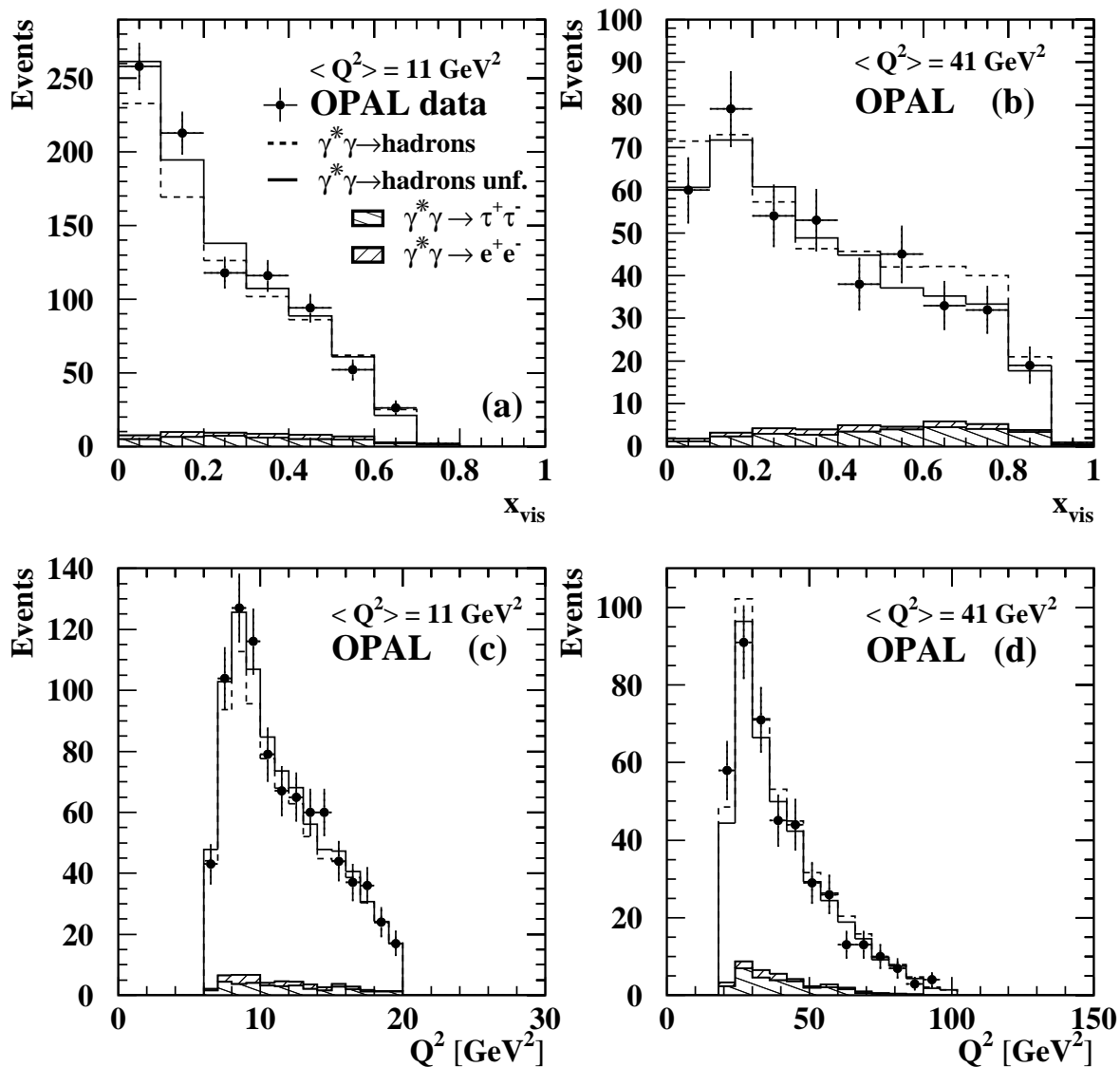


Figure 2: The x_{vis} , (a) and (b), and Q^2 , (c) and (d), distribution of the SW and FD samples for the data taken at $\sqrt{s_{\text{ee}}} = 161 - 172 \text{ GeV}$. The *dashed* histogram, $\gamma^*\gamma \rightarrow \text{hadrons}$, shows the events from the HERWIG Monte Carlo, using the GRV parametrisation and the standard cuts (the reference sample), with the background added, before the unfolding; the *solid* histogram, $\gamma^*\gamma \rightarrow \text{hadrons unf.}$, shows the same quantity, but reweighted based on the result of the unfolding. The background events from the reactions $\gamma^*\gamma \rightarrow \tau^+\tau^-$ and $\gamma^*\gamma \rightarrow e^+e^-$ are also shown separately at the bottom of the figure. All errors shown are statistical only.

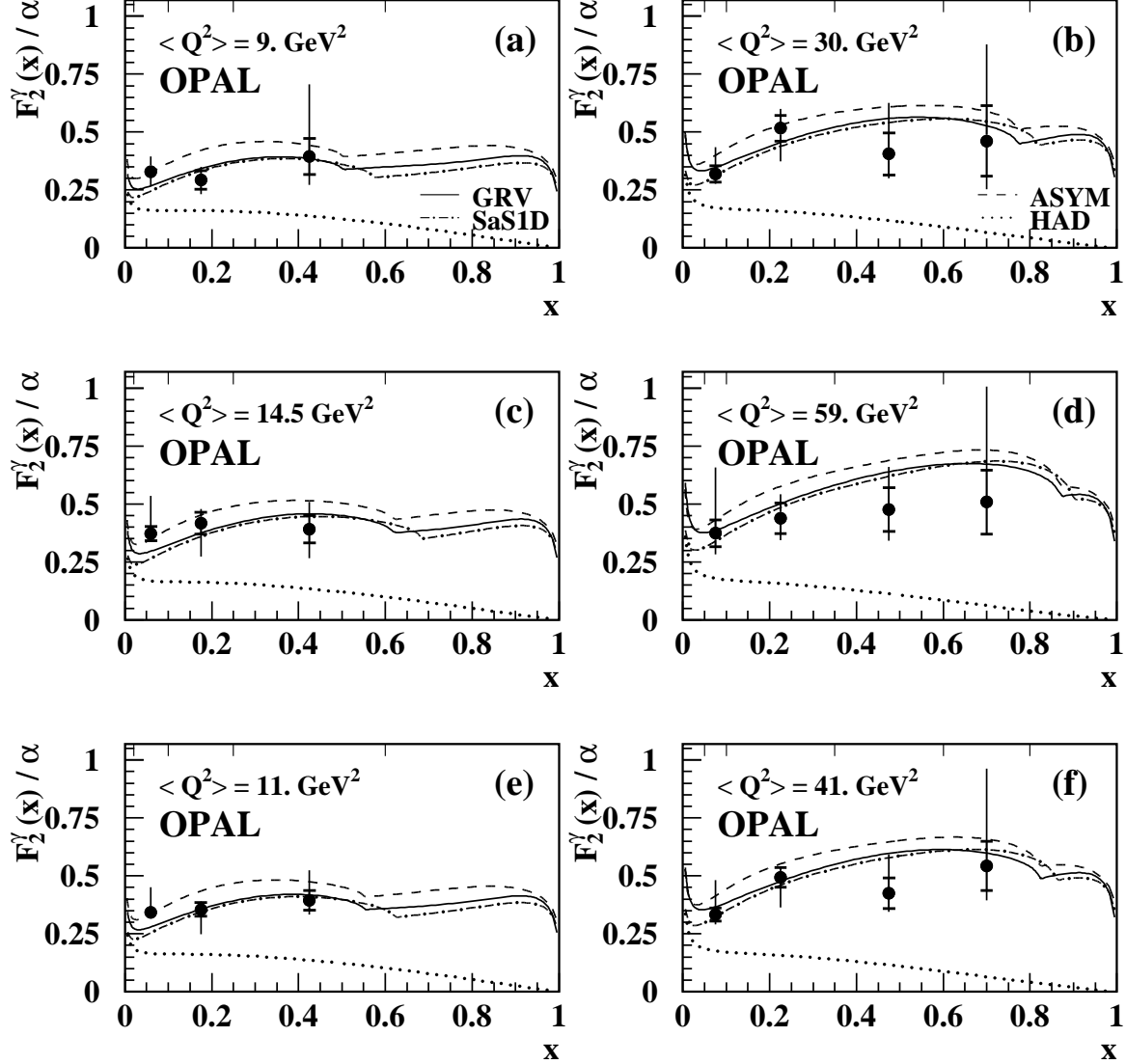


Figure 3: The measurement of F_2^γ for the data taken at $\sqrt{s_{ee}} = 161 - 172 \text{ GeV}$. The structure function F_2^γ is measured for four active flavours in four bins in Q^2 with mean values of (a) $\langle Q^2 \rangle = 9 \text{ GeV}^2$, (b) $\langle Q^2 \rangle = 30 \text{ GeV}^2$, (c) $\langle Q^2 \rangle = 14.5 \text{ GeV}^2$, and (d) $\langle Q^2 \rangle = 59 \text{ GeV}^2$. In (e) the measurement for the combined data sets of (a) and (c), and in (f) the measurement for the combined data sets of (b) and (d) is shown. The *points* show the measured F_2^γ . The bin sizes are indicated by the *vertical lines* at the top of the figure. The *solid* line represents the F_2^γ derived from the GRV parametrisation and the *dot-dashed* line denotes the F_2^γ derived from the SaS1D parametrisation, both using the Bethe-Heitler contribution to F_2^γ for massive charm quarks. The charm quark mass m_c is taken to be 1.3 GeV and 1.5 GeV in the case of SaS1D and GRV, respectively. The *dotted* line (HAD) represents the hadronic component and the *dashed* line (ASYM) the full augmented asymptotic F_2^γ , as described in the text.

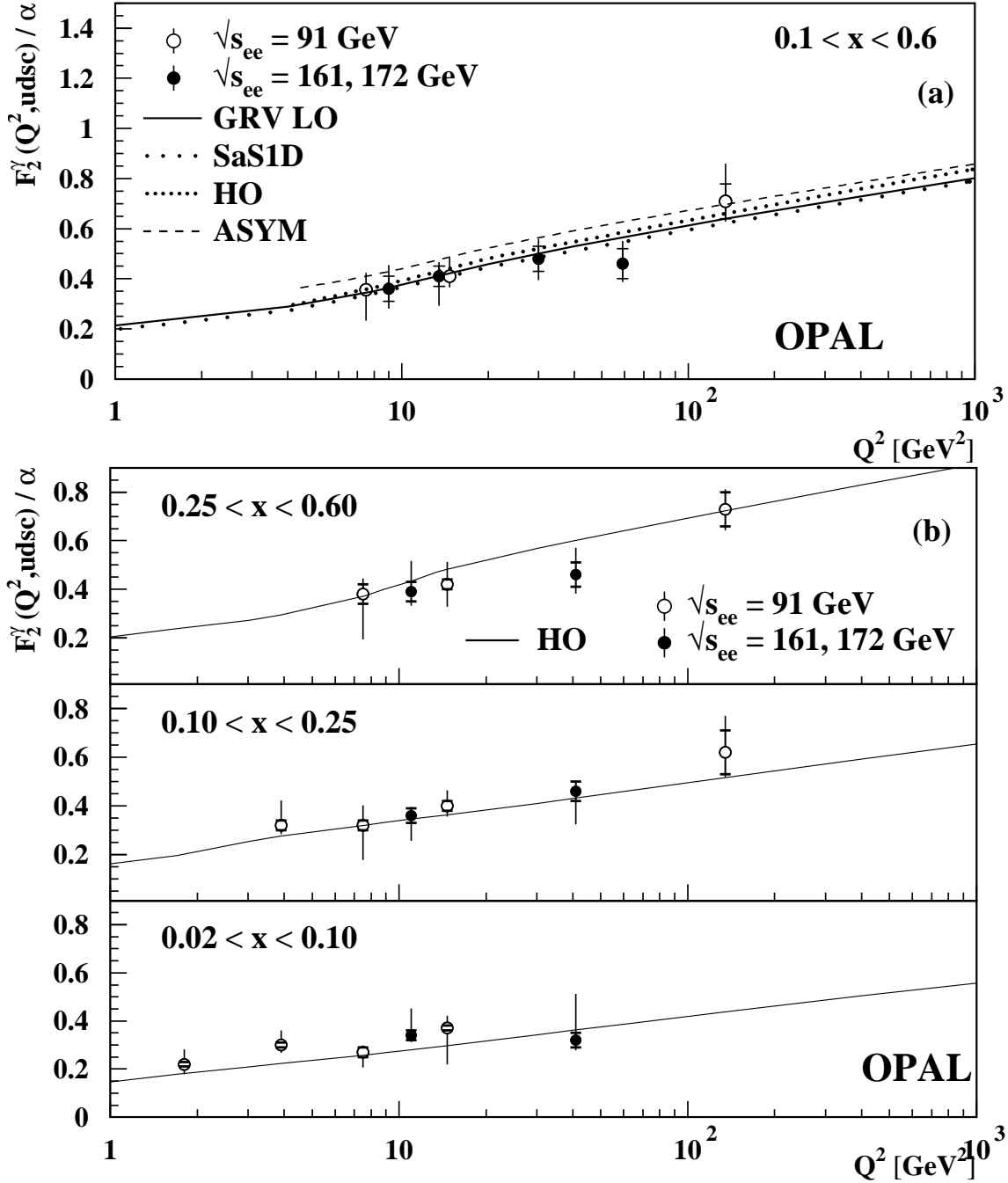


Figure 4: The measurement of F_2^γ for four active flavours as a function of Q^2 , (a) for the range $0.1 < x < 0.6$, and (b) subdivided into $0.02 < x < 0.10$, $0.10 < x < 0.25$ and $0.25 < x < 0.60$. In addition shown in (a) are the F_2^γ of the GRV (LO) and the SaS1D (LO) parametrisation, the F_2^γ of the asymptotic prediction (ASYM) and the result of a higher order calculation (HO), where the last two predictions are only shown for $Q^2 > 4$ GeV 2 . In (b) the data are only compared to the HO prediction. In both figures the errors are statistical and systematic. In some of the cases the statistical errors are not visible because they are smaller than the size of the symbols.